AGU ADVANCING EARTH AND SPACE SCIENCE

Geophysical Research Letters®

RESEARCH LETTER
10.1029/2022GL102489

Role of Oceanic Internal Instability in the Generation of Low-Frequency Variability in the Indian Ocean

S. Anjana[1,2], A. Chatterjee[1], W. Han[3], S. Prerna[1,4], and C. K. Sajidh[1,2]

[1]Indian National Centre for Ocean Information Services, Ministry of Earth Sciences, Hyderabad, India, [2]INCOIS-KUFOS Joint Centre, Kerala University of Fisheries and Ocean Studies, Kochi, India, [3]Department of Atmospheric and Oceanic Sciences, University of Colorado, Boulder, CO, USA, [4]Department of Geophysics, Banaras Hindu University, Varanasi, India

Key Points:

- High-resolution global ocean general circulation model simulation is used to document internal variability in interannual-to-longer timescale and identify processes
- Internal variability has large influence on the interannual variability of the south Indian Ocean between 20° and 40°S
- Baroclinic instability associated with the shear between the South Indian Counter Current and subsurface current drives the internal variability

Supporting Information:

Supporting Information may be found in the online version of this article.

Correspondence to:

A. Chatterjee,
abhisek.c@incois.gov.in

Citation:

Anjana, S., Chatterjee, A., Han, W., Prerna, S., & Sajidh, C. K. (2023). Role of oceanic internal instability in the generation of low-frequency variability in the Indian Ocean. *Geophysical Research Letters*, *50*, e2022GL102489. https://doi.org/10.1029/2022GL102489

Received 12 JAN 2023
Accepted 17 APR 2023

Author Contributions:

Conceptualization: S. Anjana, A. Chatterjee, W. Han
Data curation: S. Prerna
Formal analysis: S. Anjana, A. Chatterjee, S. Prerna
Investigation: S. Anjana, C. K. Sajidh
Methodology: S. Anjana, A. Chatterjee
Software: S. Prerna, C. K. Sajidh
Supervision: A. Chatterjee, W. Han
Validation: S. Anjana
Visualization: S. Anjana, C. K. Sajidh
Writing – original draft: S. Anjana, A. Chatterjee
Writing – review & editing: S. Anjana, A. Chatterjee, W. Han

Abstract Low-frequency (Interannual and longer timescale) variability in sea surface temperature (SST) of the Indian Ocean plays a crucial role in affecting the regional climate. Using a high-resolution global model simulation, we show that internal oceanic variability is an important cause of the observed low-frequency variability in the subtropical-midlatitude south Indian Ocean (SIO) between 20° and 40°S, a marked southward shift in the latitude band of active internal variability for the low-frequency compared to earlier estimates based on coarser Indian Ocean regional models. Notably, we show that internal variability does not contribute to the observed low-frequency variability in the Seychelles–Chagos thermocline ridge region. Energy budget analysis shows that baroclinic instability is the primary cause for the internal variability. The slowly growing baroclinic instabilities at low frequency and longer length scale favor Rossby waves' generation, propagating the SST and sea level anomaly signals westward.

Plain Language Summary Ocean internal variability refers to the intrinsic variability arising from nonlinearity of the oceanic system. Considering that the internal variability is not tied with the external forcing, occurrence of internal variability limits the predictability of the oceanic system. Here, we use an eddy-resolving high-resolution ocean general circulation model to document the internal variability of sea surface temperature (SST) and sea level in the Indian Ocean on interannual-to-longer timescale (referred to as low-frequency) and understand the processes that drive these variabilities. We show that internal variability in the low-frequency band has large influence on SST and sea level in the south Indian Ocean in the latitude range of 20° and 40°S, and it is primarily caused by the baroclinic instability associated with the vertical shear between the surface eastward flow of South Indian Counter Current and the subsurface westward flow of Southern Ocean supergyre.

1. Introduction

Internal climate modes and external forcing cause strong interannual-to-decadal fluctuations (hereafter collectively referred to as low-frequency variabilities) in the Indian Ocean sea surface temperature (SST) (Behera & Yamagata, 2003; Klein et al., 1999; Saji et al., 1999; Webster et al., 1999) and sea level (Han et al., 2017, 2019; Stammer et al., 2013). These variabilities show strong regional differences (Lee & McPhaden, 2008). For example, the north Indian Ocean (NIO; north of 5°S) exhibits a basin-wide fall in sea level (Srinivasu et al., 2017; Thompson et al., 2016) and upper ocean heat content (Li et al., 2018) during 1993–2003 and a rapid rise thereafter. In contrast, the south Indian Ocean (SIO; 5°–40°S) shows substantial low-frequency variability. Levitus et al. (2012) documented this hemispheric asymmetry, with the south Indian Ocean accumulating more heat than its northern counterpart and the associated decadal variability. Observational evidence and the model studies suggest that these low-frequency variabilities in the SIO are primarily forced by winds over the Indian Ocean (e.g., Nidheesh et al., 2013; Srinivasu et al., 2017; Thompson et al., 2016; Trenary & Han, 2013), atmospheric teleconnection from the western Pacific (Alexander et al., 2002) and remote forcing from the tropical Pacific via the Indonesian throughflow and subsequent Rossby wave radiations (e.g., Kataoka et al., 2014; Nagura & McPhaden, 2021; Trenary & Han, 2013; Zhuang et al., 2013).

In addition to the air-sea interaction associated with the climate modes, the oceanic internal variability due to nonlinearity of the oceanic system can also cause variabilities in a wide frequency spectrum. The oceanic internal variability is shown to contribute significantly to the observed intraseasonal-to-interannual frequency bands of the western Indian Ocean (Chatterjee et al., 2013; Jochum & Murtugudde, 2005), the South Equatorial Current

(SEC) region (Feng & Wijffels, 2002; Jochum & Murtugudde, 2005; Ogata & Masumoto, 2010, 2011), along the 20°–30°S latitudinal band of SIO interior and off the west coast of Australia (Jia, Wu, & Qiu, 2011; Jia, Wu, Lan & Qiu, 2011; Trenary & Han, 2012). Earlier modeling efforts that studied intrinsic internal variability of the Indian Ocean primarily relied on simpler and coarser-resolution regional models (Chatterjee et al., 2013; Jochum & Murtugudde, 2005; Trenary & Han, 2013), which cannot realistically resolve oceanic mesoscale variabilities driven by intrinsic instabilities. Further, the proximity of lateral boundaries of the regional models, which are often close to the region of active intrinsic variability, limits the fidelity of the modeling framework for such studies.

Here, we investigate the role of oceanic internal variability in generating low-frequency variability of the Indian Ocean SST and sea level, with a particular focus on the south Indian Ocean, using a high-resolution global ocean general circulation model (OGCM). The model configuration and experiments are discussed in Section 2. The results are presented in Section 3, and finally, Section 4 concludes our findings.

2. Ocean Model, Experiments and Observation Data Sets

This study uses a global ocean general circulation model based on the Modular Ocean Model (MOM version 5; Griffies, 2012). It uses a global tripolar grid (Murray, 1996), with model equations discretized using Arakawa-B staggered gridding and assumes hydrostatic and Boussinesq approximations. The model's horizontal resolution is eddy-permitting and is set to uniform 1/8°. In the vertical, it uses 42 geopotential levels (z-star), with the top 22 levels confined within the first 200 m of the water column. Such high horizontal and vertical resolutions allow realistic simulation of mean circulation and eddy activities in the SIO and Antarctic Circumpolar Current (ACC) regime (Figure S1 in Supporting Information S1). However, model uses a submesoscale parametrization to represent the unresolved submesoscale variabilities. More details about the model configuration are provided in Supporting Information S1.

In order to understand the role of internal variability in the generation of low-frequency variability, the model is first forced by 6-hourly climatological surface atmospheric fluxes from CORE-II climatological forcing (Large & Yeager, 2009). The climatological simulation is carried out for 175 years from a state of rest, and only the last 50 years of simulation (126–175) are analyzed in the study to avoid the initial spin-up period. Hereafter this climatological simulation is referred to as CLIM. The model is further integrated forward using 3-hourly interannual forcing from JRA55do (Tsujino et al., 2018) for 1958–2017 and is referred to as CTRL. However, to avoid spin-up transient variabilities in the CTRL simulation owing to the switch in the model forcing, only the 1962–2017 period is analyzed.

In the subsequent sections, we will frequently use anomalies of the model simulated variables like Sea Surface Temperature (SST), sea surface height (SSH), and D20 (depth of the 20°C isotherm; representative of the depth of the thermocline) to refer the eddy fields. These anomalies for CLIM and CTRL solutions are calculated by removing the average annual cycle derived using the last 50 years of CLIM simulations (126–175th climatological years) and then low-passed with a 15-month fifth-order Butterworth filter. Further, the eddy kinetic energy (EKE) is calculated based on these low-passed zonal and meridional velocity anomalies from the CLIM solution.

To document the observed variability in the SIO, we use SST from Hadley Centre Sea Ice and Sea Surface Temperature data set (HadISST) and sea level anomaly from Archiving, Validation and Interpretation of Satellite Oceanographic (AVISO). To maintain consistency with the CTRL simulation, SST observation for the period 1962–2017 is considered for all the analyses. However, for the sea level anomaly, the entire available gridded altimeter record during 1993–2021 is used.

3. Results

The observed variability in the Indian Ocean is a combined response to surface forcing and oceanic internal variability. The standard deviation maps of observed SST anomaly (SSTA) for the period 1962–2017 and Sea Level anomaly (SLA) for the period 1993–2021 at interannual and longer timescales (15-month lowpass filtered) show strong variability in the SIO (Figures 1a and 1b). Strong SSTA variability is mainly confined between 10°–38°S across the SIO basin and along the Antarctic Circumpolar Current (ACC) front, also known as subtropical front (STF), around 40°S. The variability is much weaker in the north Indian Ocean except along the Somali and Arabian

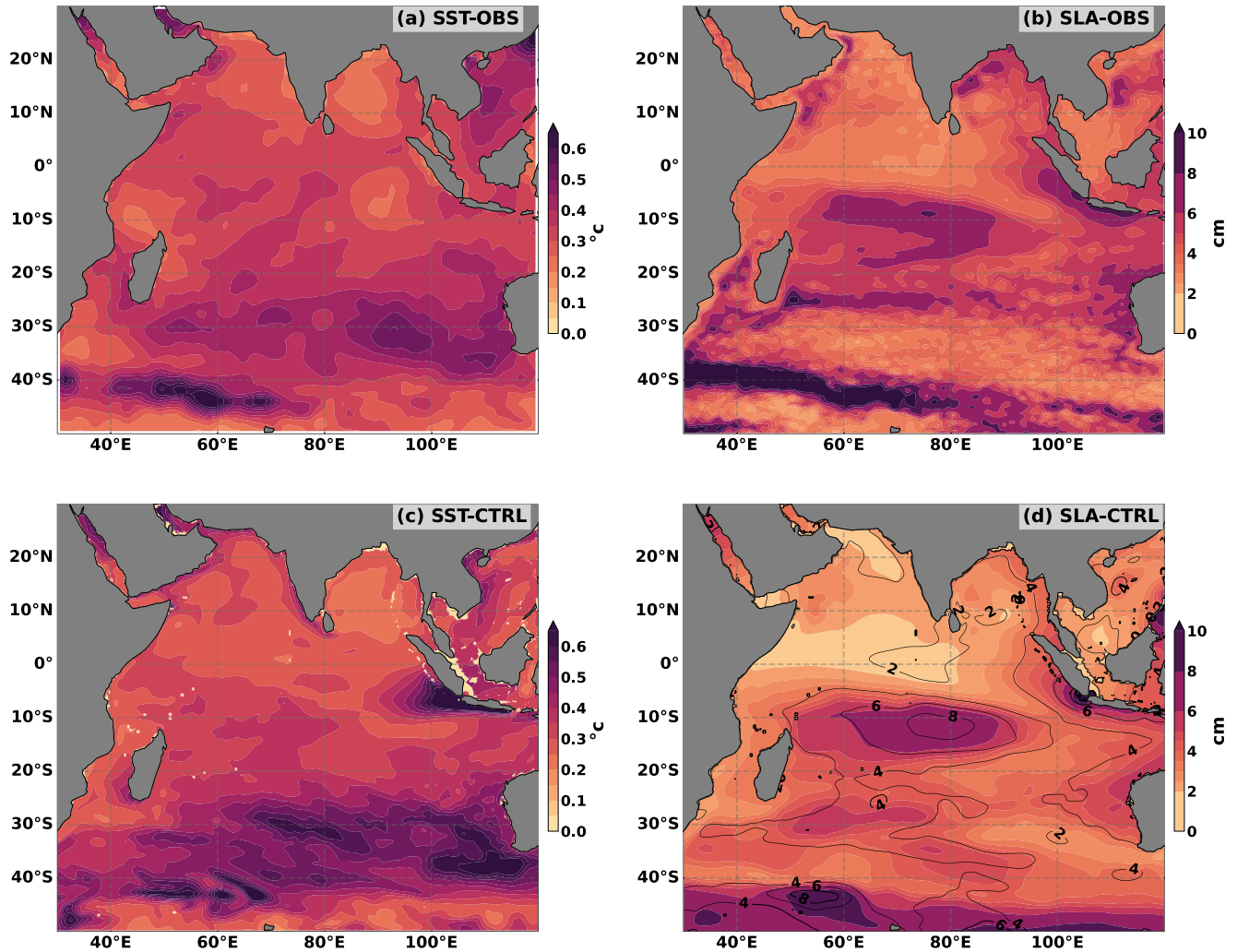

Figure 1. (a and b) are the standard deviation of observed SST (HadISST) for the period 1962–2017 and SLA (AVISO) for the period 1993–2021 (c and d) are the model simulated (CTRL) SST and SLA from 1962 to 2017. The overlayed line contour in Panel (d) shows that standard deviation of sea level for the period 1993–2017 (equivalent to the observation period). Standard deviation is calculated after removing the annual cycle and then filtered with a 15-month lowpass filter.

coasts, which has been attributed primarily to the meridional migration of Southern Gyre and Great Whirl driven by the interannual variability of summer monsoon winds and the embedded instability in the mean current system (Beal & Donohue, 2013; Chatterjee et al., 2013; Jochum & Murtugudde, 2005; Wirth et al., 2002). In contrast, standard deviation of SLA shows very distinct spatial heterogeneity, with the largest amplitude occurring along the STF region near the 40°S latitude band. In the SIO, variability is confined to three distinct regions: over the Seychelles−Chagos thermocline ridge region between 5°−20°S (Hermes & Reason, 2008; Yokoi et al., 2008), in the subtropical basin between 20°−30°S and along the southwestern boundary of Australia. Additionally, strong low-frequency variability exhibits along the west coast of Sumatra and Java between 5°−10°S. While the interannual variability along the Sumatra and Java coast is primarily driven by equatorial winds and the alongshore winds associated with dominant climate modes (e.g., Cao et al., 2018; Du et al., 2008; Saji et al., 1999; Susanto et al., 2001; Vinayachandran et al., 2021), variability along the STF is driven by Southern Annual mode and the instability generated due to bottom torque associated with the ACC (Boer et al., 2013). In the NIO, SLA variabilities co-locate with the SSTA along the western boundary of the Arabian Sea. The other region of relatively active interannual variability of sea level is the eddy-dominated Bay of Bengal (Mukherjee et al., 2019; Philips et al., 2021 and the references therein).

In this paper, we focus on the SSTA and SLA, which show large amplitude variability across the tropical-subtropical SIO, where the role of oceanic internal variability in causing low-frequency variability is not well documented.

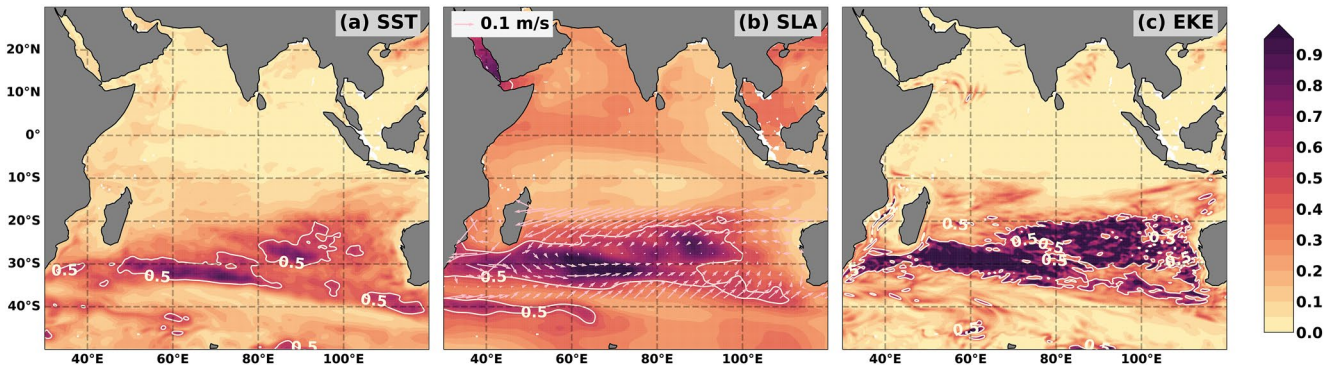

Figure 2. The ratio of the standard deviations of (a) sea surface temperature, (b) sea level anomaly and (c) eddy kinetic energy derived from CLIM (last 50 years i.e., 126–175 years) and CTRL (1962–2017) simulation overlaid by a contour of 0.5. Standard deviation is calculated after removing the annual cycle and then filtered with a 15-month lowpass filter. The vectors overlayed in Panel (b) represents mean surface currents highlighting SEC and SICC in the SIO.

Figure 1 shows the standard deviations of SSTA and SLA from the CTRL solution for the 1962−2017 period. Note that the CTRL simulation is the complete solution, which includes both forced response and internal variability. The model could reasonably reproduce the observed variability over the Indian Ocean, particularly for the regions of high variabilities in the SIO. However, there are a few notable differences. The overall model simulated SSTA shows stronger variability than the observation. This is particularly visible along the Java coast, where the model produces much stronger variability than the observation, likely due to the shallower MLD and thus stronger SSTA response to wind forcing in the model. In contrast, variability in model SLA is generally weaker across the domain. Nevertheless, the model is able to simulate major features of the SSTA and SLA variability across the entire basin for further analysis.

3.1. Internal Oceanic Variability

In order to understand the role of internal oceanic variability in generating low-frequency SST and sea level variability, we compare solutions from CLIM and CTRL simulations. Considering that surface fluxes that force experiment CLIM do not have any variability longer than the annual period, and thus any low-frequency signals with periods longer than the annual period is due to low-frequency rectification of the oceanic internal instabilities. Figure 2 shows the ratio of the standard deviations of anomalies of SST, SLA and EKE from CLIM and CTRL simulations. The regions where the ratio between the internal variability from CLIM and "total" variability from CTRL is more than 0.5 are considered largely influenced by internal variability, because the magnitude of internal variability exceeds 50% of the total variability and is comparable to the atmospheric forcing in generating the low-frequency variability.

Ratios for both SSTA and SLA (Figures 2a and 2b) show large influence of internal variability in regions between 20°–40°S, starting from the eastern SIO off the west Australian coast to the western basin with maximum strength occurring in a region southeast of Madagascar. In fact, this is the region where strong variability in observed SST was noted (see Figure 1a). D20 anomaly also shows active regions of interannual variability co-locating with the strong SLA (figure not shown), supporting the dynamic nature involved in the oceanic internal variability. The ratio of the EKE provides a clear picture of two dynamically distinct regions: the region off the west coast of Australia driven by Leeuwin current/under current and its offshore extension associated with Rossby wave radiations (Furue et al., 2017; Rennie et al., 2007) and the eastward flowing South Indian Counter Current (SICC) regime at ∼30°S in the southeast of Madagascar (Figure 2c). These suggest that the generation of instabilities driven by the unstable seasonal mean current may have distinct dynamical nature in the eastern and western parts of the SIO. Furthermore, it is noteworthy that the internal variability does not contribute to the SSTA and SLA Seychelles−Chagos thermocline ridge region and near the Indonesian coast, indicating that the observed variability in these regions is primarily driven by the direct surface forcing.

3.2. Energy Budget and Instabilities

We further investigate the generation mechanisms of the internal variability through an eddy kinetic energy budget analysis following Masina et al. (1999) and Chatterjee et al. (2013). To calculate the EKE using the

solution from CLIM simulation, each field is separated into time mean (overbar) and perturbation (prime). In this case, the mean field is the forced response, that is, annual signal, and the perturbation is its anomaly. In other words, interannual and longer period (period >15 months) variabilities are represented as perturbations or eddy fields. Note that the eddy EKE can also be contributed from the rectification by higher frequency variability (periods <15 months); this effect however is negligible compared to the EKE from low frequency variability. The EKE budget is given by

$$K_{\mathrm{et}} + \underbrace{\overline{\boldsymbol{V}}\cdot\nabla K_e + \overline{w}K_{\mathrm{ez}}}_{A} + \underbrace{\boldsymbol{V}'\cdot\nabla K_e + w'K_{\mathrm{ez}}}_{B} = \underbrace{-\nabla\cdot\left(\boldsymbol{V}'p'\right) - \left(w'p'\right)_z - g\rho'w'}_{C} + \underbrace{\rho_o\left[-\boldsymbol{V}'\cdot\left(\boldsymbol{V}'\cdot\nabla\overline{\boldsymbol{V}}\right) - \boldsymbol{V}'\cdot\left(w'\overline{\boldsymbol{V}}_z\right)\right]}_{D}$$
$$+\underbrace{\rho_o\left[\boldsymbol{V}'\cdot\left(\boldsymbol{V}'\cdot\nabla\boldsymbol{V}'\right) + \boldsymbol{V}'\cdot\left(w'\boldsymbol{V}'_z\right)\right]}_{E} + \underbrace{\left[A_{\mathrm{MH}}\left(\boldsymbol{V}'\cdot\nabla^2\boldsymbol{V}'\right) + \boldsymbol{V}'\cdot\left(A_{\mathrm{MV}}\boldsymbol{V}'_z\right)_z\right]}_{F},$$

where, K_e is the EKE, ∇ represents horizontal gradient, and A_{MH} and A_{MV} are the horizontal and vertical viscosity coefficients. The first term on the left side of the equation is the local rate of change of EKE, the terms A and B represent the horizontal and vertical advection of EKE by mean and perturbation flows. The first two terms in C represent divergence by pressure anomaly, and the last term represents the conversion of available eddy potential energy into EKE (a measure of baroclinic instability). The first term of D describes the energy conversion via barotropic instability and the second term is the energy conversion due to vertical shear in the mean-field, also referred to as Kelvin-Helmholtz instability. Term E is the deformation of work due to the perturbed velocity field, and term F is the dissipation of EKE. Note that except for the baroclinic conversion term, and to some extent the barotropic conversion and horizontal advection of EKE, all other terms of the equation are very small in this region and, therefore, are not considered further.

Figure 3 illustrates the seasonal average of EKE for austral summer (January−March), autumn (April−June), winter (July−September) and spring (October−December) and the dominant instability terms. The distribution of EKE shows strong spatial and temporal heterogeneity. Moreover, regions of strong eddy activity co-locate well with the areas where the internal variability is large (see Figure 2). Throughout the year, strong EKE is found along the southern branch of the SICC south of Madagascar at ∼30°S, and to a lesser extent in the central interior basin of SIO between 20°−30°S, and their magnitudes are somewhat stronger during austral spring and summer (Figure S2 in Supporting Information S1). Off the west coast of Australia, EKE intensifies during austral fall and peaks in winter. A similar strong seasonal EKE along 25°S during summer in the east-central SIO was earlier reported by Palastanga et al. (2007) and Jia, Wu, and Qiu (2011). They showed that vertical shear of eastward flowing surface SICC and underlying westward flowing SEC, associated with meridional isopycnal tilt, cause water column baroclinically unstable with the strongest growing mode in intraseasonal/seasonal periodic band and at mesoscale wavelength (∼200−500 km). In comparison, strong eddy activity with a westward phase propagation at intraseasonal timescale is documented during winter in the eastern part of the SIO (Feng & Wijffels, 2002; Zhou et al., 2008) and off the Leeuwin Current/Leeuwin Undercurrent region near the west coast of Australia (Birol & Morrow, 2001; Furue et al., 2017; Morrow et al., 2003; Rennie et al., 2007). Note here that while our analysis shows similar EKE dominated regions in the SIO, the EKE calculated here is from the CLIM experiment and thus isolates the effect of ocean internal variability at timescales longer than the annual period. This low-frequency variabilities of SST and sea level result from energy cascade from seasonal mean flow to lower frequency bands. Further analysis based on the EKE budget equation suggests that, among all the energy conversion terms, baroclinic instability ($-g\rho'w'$) is the most dominating term in the SIO. In fact, as observed in EKE, baroclinic instability also shows a similar spatial heterogeneity with the strongest amplitude co-locating with the strong EKE region (Figure 3). In contrast, while barotropic instabilities have been suggested to be important in some regions of the SIO on intraseasonal and seasonal timescales (e.g., south of Madagascar; Halo et al., 2014; Yamagami et al., 2019), they are negligible at inter annual and longer timescales. These instabilities get advected to the east in the interior basin by the eastward surface SICC, particularly along the 30°S latitude belt.

3.3. Dynamical Mechanisms

Seasonal variation of thermocline structure has been suggested to be related to the generation of baroclinic instability in the eastern SIO (Feng & Wijffels, 2002; Jia, Wu, & Qiu, 2011). Here, we adopted a similar technique

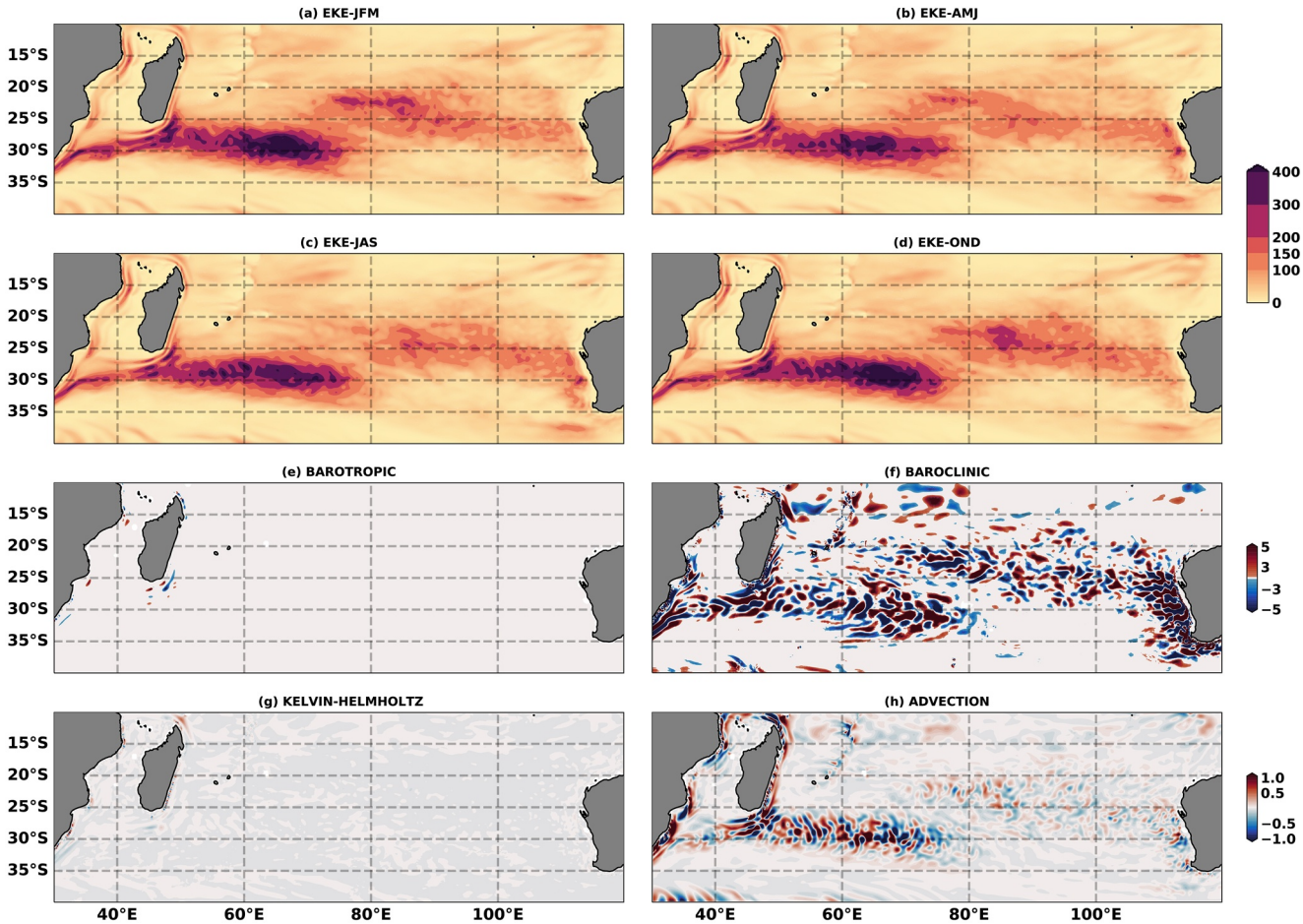

Figure 3. Eddy kinetic energy (EKE; 10^{-4} kg s^{-3}) from CLIM solution for the four seasons: (a) summer (January–March), (b) fall (April–June), (c) winter (July–September), (d) spring (October–December). (e) are the barotropic energy conversion (10^{-4} kg s^{-3}), (f) baroclinic energy conversion (10^{-4} kg s^{-3}), (g) Kelvin-Helmholtz (10^{-4} kg s^{-3}) and (h) advection (10^{-4} kg s^{-3}) averaged for the entire period and are integrated over the top 200 m water column. Note that the scale for Kelvin-Helmholtz conversion and advection is smaller than the baroclinic and barotropic terms as they contribution from these terms are considerably weaker.

to identify the source of energy conversion in low-frequency spectrum through baroclinic instability across the regions of active EKE.

Isotherms in the SIO show strong seasonal variability, particularly in the top 200 m water column. In the interior SIO, during austral summer, the isothermal layers are shallow, generally limited within the top 50 m and extend poleward across the SIO (Figure 4a: January; Figure S3 in Supporting Information S1). As a result, the out-cropped isotherms tilt poleward south of 25°S, thereby increasing meridional gradient of density below the isothermal layer and thus, based on thermal wind relation, enhancing the vertical shear of eastward flowing SICC. These isothermal tilts lead to strong baroclinic instability, which draws energy from the mean seasonal tilt of the thermocline to enhance the EKE of the region. The tilt angle reverses to equatorward between 25°–15°S, causing the thermocline to shoal there. This region is marked by strong baroclinicity with an eastward flowing surface SICC and an underlying westward flow associated with the northern branch of the subtropical gyre (Furue et al., 2017; Schott et al., 2009) or the southern hemispheric supergyre (Ridgway & Dunn, 2007; Speich et al., 2007). The splitting of surface SICC into two branches near 30° and 25°S was documented earlier by Menezes et al. (2014). During winter, isotherms migrate equatorward, and the isothermal layer becomes deeper than 100 m (Figure 4a, Figure S3 in Supporting Information S1) across the SIO. This is particularly conspicuous south of 25°S, where it deepens to more than 200 m. Additionally, eastward flowing SICC in the south (30°S) and westward flowing SEC in the north (~15°S) deepen and subsequently weakens the vertical shear of the zonal current and associated EKE in the upper water column.

The other region that exhibits strong EKE is the southwest coast of Australia. But unlike the rest of the SIO, EKE strengthens here during austral fall and attains its maximum during winter (Figures 3b and 3c and Figure S4 in

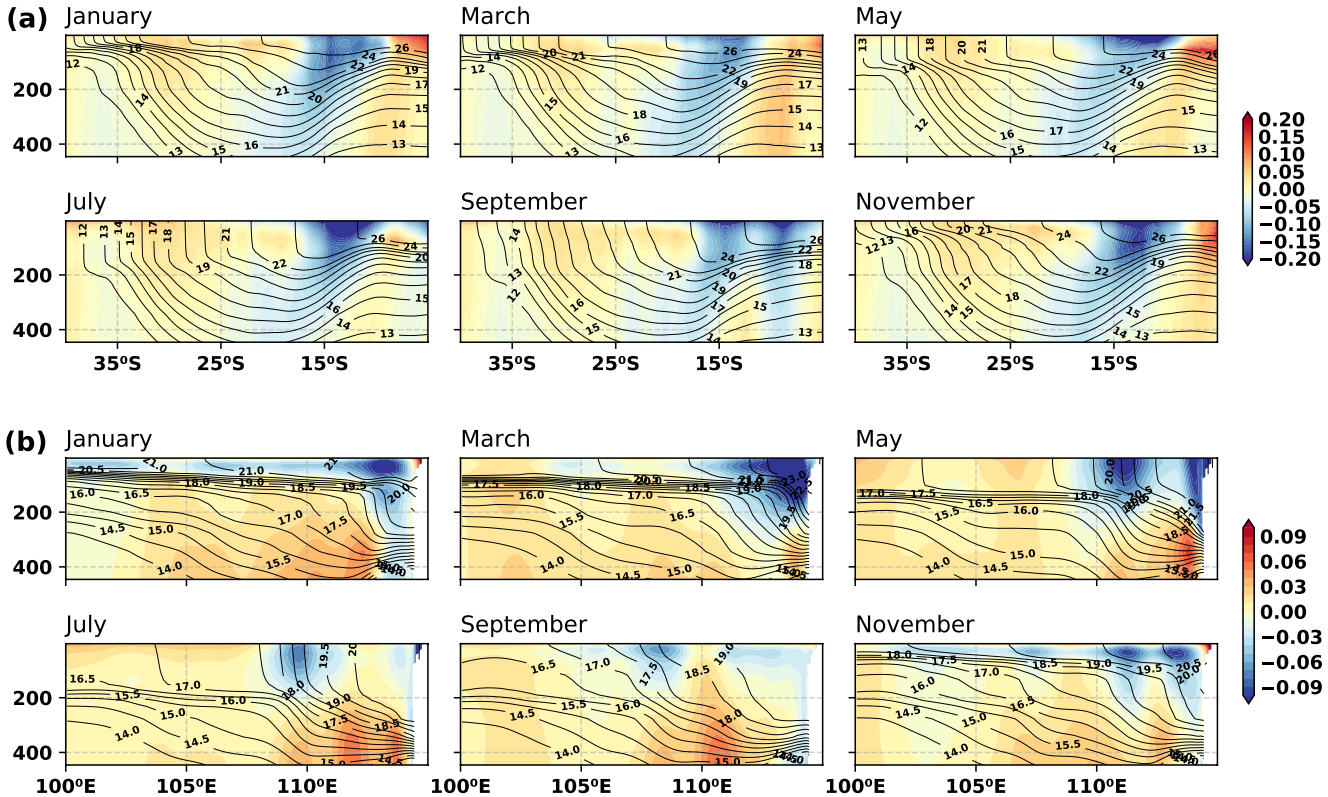

Figure 4. (a) Vertical sections of climatological zonal currents (shaded) and temperature (contour) averaged over 60°−100°E in the interior south Indian Ocean. (b) Vertical section of climatological meridional current (shaded) and temperature (contour) averaged at 30°S off the west coast of Australia. Note that all the climatological fields are derived from averaging the last 50 years of simulation (126–175) from CLIM experiment.

Supporting Information S1). Finally, EKE disappears during summer. The increase of EKE in fall is associated with the strengthening of the poleward Leeuwin Current and the underlying Leeuwin undercurrent (Figure 4b) (Feng & Wijffels, 2002; Furue et al., 2017). This causes a very strong vertical shear and isotherms to tilt offshore. As a result, the water column becomes baroclinically unstable, resulting in anti-cyclonic surface intensified eddies in the Leeuwin Current and cyclonic eddies in the Leeuwin Undercurrent (Rennie et al., 2007). Finally, these eddies propagate westward as Rossby waves (Figure S5 in Supporting Information S1) (Feng & Wijffels, 2002; Schouten et al., 2002a, 2002b; Rennie et al., 2007). By summer, the strengths of the Leeuwin Current and Leeuwin Undercurrent become minimum and thus weaken the vertical shear and the associated thermocline tilt.

3.4. Scale Selection

While it is clearly demonstrated that the internal oceanic variability plays an important role in causing the low-frequency variability of SST and sea level in the SIO, whether the baroclinic instability can grow at interannual and longer timescales and generate the low-frequency variability is unclear. Note that baroclinic instability at short timescales (e.g., intraseasonal) can also rectify into interannual and longer term variability due to nonlinearity of the oceanic system. Here, we discuss possible mechanisms for the low-frequency instability to grow.

It has been shown that the vertical shear between the eastward flowing shallow SICC and the underlying westward flow associated with the southern hemispheric supergyre is due to the seasonal variation of thermocline tilt and therefore, baroclinic instability in the upper water column in the interior SIO. Jia, Wu, Lan, and Qiu (2011) earlier noted that, using a 2.5 layer quasi-geostrophic reduced-gravity model, instabilities owing to the vertical shear can grow at a wide range of the spectrum (Figure 8 of their paper), but they are associated with specific preferred zonal and meridional length scales. Instability can grow rapidly with an e-folding timescale of 100–200 days with a zonal length scale of ∼O(200) km, but a much larger meridional length scale of ∼O(1,000) km. On the other hand, instabilities can also grow slowly at interannual to longer e-folding timescales, but with a much larger zonal length scale of ∼O(1,000) km and a smaller meridional length scale of ∼O(200) km.

The region of strong baroclinic instabilities in the interior SIO is much narrow in meridional direction compared to the zonal (∼10°−20°) extent (Figure 4). Thus, they are associated with a slower growth rate, and larger zonal-scale interannual to longer timescale instabilities. These slowly growing instability modes fit well with the lower-order modes of the Rossby waves of similar wavelength and frequency. In fact, the propagation speed of these low-frequency phases is estimated to be around 2.5–3.0 cm/s (Figure S5 in Supporting Information S1) which agrees well with the theoretical speed of the first baroclinic mode of Rossby waves at these latitudes given by $\beta c_n^2 / f^2$ (Figure S5c in Supporting Information S1), where β is the meridional rate change of the Coriolis parameter f and c_n is the characteristic speed of the n'th vertical mode gravity waves. Further, it can also be seen that at 25°S, the westward propagation of phases radiates from the east and is most prominent within the east of 80°E (Figure S5 in Supporting Information S1). Whereas, at 30°S, the westward Rossby wave propagation is evident mainly west of 80°E. These spatial heterogeneities in Rossby wave propagation at different latitude bands correspond well with the region of active baroclinic instability observed earlier (see Figure 3). This supports that the baroclinic instability-driven internal variability in the low-frequency spectrum in the SIO is likely due to the preferentially growing instability mode.

4. Conclusions

In this study, we investigate the role of oceanic internal variability in the observed interannual and near-decadal variability of the Indian Ocean using a high–resolution global MOM5 model simulations. CLIM simulation shows strong interannual to near-decadal variability in the 10°–40°S latitude band of the Indian Ocean (SIO). Considering that the annual atmospheric variability only forces the CLIM solution, the simulated low-frequency variability is driven by the internal oceanic variability. However, internal variability exhibits a strong spatial and temporal heterogeneity across this region. The modulation of isothermal tilts associated with vertical shear of the geostrophic zonal currents results in a baroclinically unstable upper water column, leading to enhanced EKE of this region. The SIO exhibits three distinct active low-frequency EKE regions: south of 25°S in the west, between 25°−15°S in the east-central basin and on the southwest coast of Australia. While the vertical shear in the eastward SICC associated with a strong thermocline tilt is responsible for the baroclinic instability in the southwest, the baroclinic zonal current with eastward flowing surface SICC and underlying westward current associated with supergyre cause vertical shear and baroclinic instability in the central interior basin. Along the southwest coast of Australia, EKE attains its peak during winter and is modulated by the strength of the Leeuwin Current and Leeuwin Undercurrent system. These instabilities then preferentially grow for the zonal scale of ∼1,000 km with an e-folding timescale of interannual periods and, thus, cause low-frequency variability in the SIO latitudinal band. Further, as these disturbances match the scale of the lower-order modes of Rossby waves, they propagate westward, carrying the energy to the western part of the basin.

Notably, earlier Jochum and Murtugudde (2005) reported that the region of active internal variability in the low-frequency spectrum is the SEC regime between 10°−20°S, which is north of active internal variability region found in this study. The most likely reason for this discrepancy is due to their simpler regional model configuration with closed southern and eastern boundaries at 25°S and 130°E, respectively. This indicates that the influence of the Pacific that feeds the SEC and the Southern Ocean, which force the SICC and supergyre, and thereby, the baroclinicity in the SIO, is the key to the observed internal variability of this region.

Since the internal variability is known to influence surface variables, it can impact the air-sea interactions such as the Subtropical Indian Ocean Dipole (SIOD) and possibly the Southern Annual Mode and predictability of the regional climate. Hence, further analysis is needed to understand the implication of these internal variabilities to the regional climate through a fully coupled atmosphere and ocean modeling experiments.

Data Availability Statement

Hadley Centre Sea Ice and Sea Surface Temperature data set (HadISST) used here are freely available at Met Office Hadley Centre observations datasets via https://www.metoffice.gov.uk/hadobs/hadisst/. AVISO data used here is available from https://doi.org/10.48670/moi-00148. All the figures are prepared using Python version 3.8.5 (https://www.python.org).

Acknowledgments
This work is funded by the "Deep Ocean Mission" programme of the Ministry of Earth Sciences, Government of India. AS acknowledges the support provided by the Department of Science and Technology for the "INSPIRE" fellowship. WH is partially supported by National Science Foundation award NSF-AGS 1935279 and NASA Ocean Surface Topography Science Team award 80NSSC21K1190. CKS acknowledges the financial support provided by Council of Scientific and Industrial Research (CSIR). This is INCOIS contribution no. 491.

References

Alexander, M. A., Bladé, I., Newman, M., Lanzante, J. R., Lau, N., & Scott, J. D. (2002). The atmospheric bridge: The influence of ENSO teleconnections on air–sea interaction over the global oceans. *Journal of Climate*, *15*(16), 2205–2231. https://doi.org/10.1175/1520-0442(2002)015<2205:tabtio>2.0.co;2

Beal, L. M., & Donohue, K. A. (2013). The Great Whirl: Observations of its seasonal development and interannual variability. *Journal of Geophysical Research: Oceans*, *118*(1), 1–13. https://doi.org/10.1029/2012jc008198

Behera, S. K., & Yamagata, T. (2003). Influence of the Indian Ocean Dipole on the Southern Oscillation. *Journal of the Meteorological Society of Japan. Series II*, *81*(1), 169–177. https://doi.org/10.2151/jmsj.81.169

Birol, F., & Morrow, R. (2001). Source of the baroclinic waves in the southeast Indian Ocean. *Journal of Geophysical Research*, *106*(C5), 9145–9160. https://doi.org/10.1029/2000jc900044

Cao, G., He, Y., Wei, Z., & Xu, T. (2018). Interannual modulation of intraseasonal sea level variability along the southern coast of Java. *Science China Earth Sciences*, *61*(1), 1–12. https://doi.org/10.1007/s11430-017-9106-0

Chatterjee, A., Shankar, D., McCreary, J. P., Jr., & Vinayachandran, P. N. (2013). Yanai waves in the Western equatorial Indian Ocean. *Journal of Geophysical Research: Oceans*, *118*(3), 1556–1570. https://doi.org/10.1002/jgrc.20121

De Boer, A. M., Graham, R. M., Thomas, M. D., & Kohfeld, K. E. (2013). The control of the Southern Hemisphere Westerlies on the position of the subtropical front. *Journal of Geophysical Research: Oceans*, *118*(10), 5669–5675. https://doi.org/10.1002/jgrc.20407

Du, Y., Qu, T., & Meyers, G. (2008). Interannual variability of sea surface temperature off Java and Sumatra in a global GCM. *Journal of Climate*, *21*(11), 2451–2465. https://doi.org/10.1175/2007jcli1753.1

Feng, M., & Wijffels, S. (2002). Intraseasonal variability in the South Equatorial Current of the East Indian Ocean. *Journal of Physical Oceanography*, *32*(1), 265–277. https://doi.org/10.1175/1520-0485(2002)032<0265:ivitse>2.0.co;2

Furue, R., Guerreiro, K., Phillips, H. E., McCreary, J. P., Jr., & Bindoff, N. L. (2017). On the Leeuwin Current System and its linkage to zonal flows in the South Indian Ocean as inferred from a gridded hydrography. *Journal of Physical Oceanography*, *47*(3), 583–602. https://doi.org/10.1175/jpo-d-16-0170.1

Griffies, S. M. (2012). *Elements of the Modular Ocean Model (MOM)*. (Vol. 7, p. 620) GFDL Ocean group Technical Report.

Halo, I., Penven, P., Backeberg, B., Ansorge, I., Shillington, F., & Roman, R. (2014). Mesoscale eddy variability in the southern extension of the East Madagascar Current: Seasonal cycle, energy conversion terms, and eddy mean properties. *Journal of Geophysical Research: Oceans*, *119*(10), 7324–7356. https://doi.org/10.1002/2014jc009820

Han, W., Meehl, G. A., Stammer, D., Hu, A., Hamlington, B., Kenigson, J., et al. (2017). Spatial patterns of sea level variability associated with natural internal climate modes. Integrative study of the mean sea level and its components. 221–254.

Han, W., Stammer, D., Thompson, P., Ezer, T., Palanisamy, H., Zhang, X., et al. (2019). Impacts of basin-scale climate modes on coastal sea level: A review. *Surveys in Geophysics*, *40*(6), 1493–1541. https://doi.org/10.1007/s10712-019-09562-8

Hermes, J. C., & Reason, C. J. C. (2008). Annual cycle of the South Indian Ocean (Seychelles-Chagos) thermocline ridge in a regional ocean model. *Journal of Geophysical Research*, *113*(C4), C04035. https://doi.org/10.1029/2007jc004363

Jia, F., Wu, L., Lan, J., & Qiu, B. (2011). Interannual modulation of eddy kinetic energy in the southeast Indian Ocean by Southern Annular Mode. *Journal of Geophysical Research*, *116*(C2), C02029. https://doi.org/10.1029/2010jc006699

Jia, F., Wu, L., & Qiu, B. (2011). Seasonal modulation of eddy kinetic energy and its formation mechanism in the southeast Indian Ocean. *Journal of Physical Oceanography*, *41*(4), 657–665. https://doi.org/10.1175/2010jpo4436.1

Jochum, M., & Murtugudde, R. (2005). Internal variability of Indian ocean SST. *Journal of Climate*, *18*(18), 3726–3738. https://doi.org/10.1175/jcli3488.1

Kataoka, T., Tozuka, T., Behera, S., & Yamagata, T. (2014). On the Ningaloo Niño/Niña. *Climate Dynamics*, *43*(5–6), 1463–1482. https://doi.org/10.1007/s00382-013-1961-z

Klein, S. A., Soden, B. J., & Lau, N. C. (1999). Remote sea surface temperature variations during ENSO: Evidence for a tropical atmospheric bridge. *Journal of Climate*, *12*(4), 917–932. https://doi.org/10.1175/1520-0442(1999)012<0917:rsstvd>2.0.co;2

Large, W., & Yeager, S. G. (2009). The global climatology of an interannually varying air–sea flux data set. *Climate Dynamics*, *33*(2–3), 341–364. https://doi.org/10.1007/s00382-008-0441-3

Lee, T., & McPhaden, M. J. (2008). Decadal phase change in large-scale sea level and winds in the Indo-Pacific region at the end of the 20th century. *Geophysical Research Letters*, *35*(1), L01605. https://doi.org/10.1029/2007gl032419

Levitus, S., Antonov, J. I., Boyer, T. P., Baranova, O. K., Garcia, H. E., Locarnini, R. A., et al. (2012). World ocean heat content and thermosteric sea level change (0–2000 m), 1955–2010. *Geophysical Research Letters*, *39*(10). https://doi.org/10.1029/2012gl051106

Li, Y., Han, W., Hu, A., Meehl, G. A., & Wang, F. (2018). Multidecadal changes of the upper Indian Ocean heat content during 1965–2016. *Journal of Climate*, *31*(19), 7863–7884. https://doi.org/10.1175/jcli-d-18-0116.1

Masina, S., Philander, S. G. H., & Bush, A. B. G. (1999). An analysis of tropical instability waves in a numerical model of the Pacific Ocean 2. Generation and energetics of the waves. *Journal of Geophysical Research*, *104*(C12), 29637–29661. https://doi.org/10.1029/1999jc900226

Menezes, V. V., Phillips, H. E., Schiller, A., Bindoff, N. L., Domingues, C. M., & Vianna, M. L. (2014). South Indian Countercurrent and associated fronts. *Journal of Geophysical Research: Oceans*, *119*(10), 6763–6791. https://doi.org/10.1002/2014jc010076

Morrow, R., Fang, F., Fieux, M., & Molcard, R. (2003). Anatomy of three warm-core Leeuwin Current eddies. *Deep Sea Research Part II: Topical Studies in Oceanography*, *50*(12–13), 2229–2243. https://doi.org/10.1016/s0967-0645(03)00054-7

Mukherjee, A., Chatterjee, A., & Francis, P. A. (2019). Role of Andaman and Nicobar Islands in eddy formation along Western boundary of the Bay of Bengal. *Scientific Reports*, *9*(1), 1–10. https://doi.org/10.1038/s41598-019-46542-9

Murray, R. J. (1996). Explicit generation of orthogonal grids for ocean models. *Journal of Computational Physics*, *126*(2), 251–273. https://doi.org/10.1006/jcph.1996.0136

Nagura, M., & McPhaden, M. J. (2021). Interannual variability in sea surface height at Southern midlatitudes of the Indian Ocean. *Journal of Physical Oceanography*, *51*(5), 1595–1609. https://doi.org/10.1175/jpo-d-20-0279.1

Nidheesh, A. G., Lengaigne, M., Vialard, J., Unnikrishnan, A. S., & Dayan, H. (2013). Decadal and long-term sea level variability in the tropical Indo-Pacific Ocean. *Climate Dynamics*, *41*(2), 381–402. https://doi.org/10.1007/s00382-012-1463-4

Ogata, T., & Masumoto, Y. (2010). Interactions between mesoscale eddy variability and Indian Ocean Dipole events in the southeastern tropical Indian ocean—Case studies for 1994 and 1997/1998. *Ocean Dynamics*, *60*(3), 717–730. https://doi.org/10.1007/s10236-010-0304-4

Ogata, T., & Masumoto, Y. (2011). Interannual modulation and its dynamics of the mesoscale eddy variability in the southeastern tropical Indian Ocean. *Journal of Geophysical Research*, *116*(C5), C05005. https://doi.org/10.1029/2010jc006490

Palastanga, V., Van Leeuwen, P. J., Schouten, M. W., & De Ruijter, W. P. M. (2007). Flow structure and variability in the subtropical Indian ocean: Instability of the South Indian ocean countercurrent. *Journal of Geophysical Research*, *112*(C1), C01001. https://doi.org/10.1029/2005jc003395

Phillips, H. E., Tandon, A., Furue, R., Hood, R., Ummenhofer, C. C., Benthuysen, J. A., et al. (2021). Progress in understanding of Indian Ocean circulation, variability, air–sea exchange, and impacts on biogeochemistry. *Ocean Science*, *17*(6), 1677–1751. https://doi.org/10.5194/os-17-1677-2021

Rennie, S. J., Pattiaratchi, C. P., & McCauley, R. D. (2007). Eddy formation through the interaction between the Leeuwin current, Leeuwin undercurrent and topography. *Deep Sea Research Part II: Topical Studies in Oceanography*, *54*(8–10), 818–836. https://doi.org/10.1016/j.dsr2.2007.02.005

Ridgway, K. R., & Dunn, J. R. (2007). Observational evidence for a Southern Hemisphere oceanic supergyre. *Geophysical Research Letters*, *34*(13). https://doi.org/10.1029/2007gl030392

Saji, N., Goswami, B., Vinayachandran, P. N., & Yamagata, T. (1999). A dipole mode in the tropical Indian Ocean. *Nature*, *401*(6751), 360–363. https://doi.org/10.1038/43854

Schott, F. A., Xie, S. P., & McCreary, J. P., Jr. (2009). Indian Ocean circulation and climate variability. *Review of Geophysics*, *47*(1), RG1002. https://doi.org/10.1029/2007RG000245

Schouten, M. W., De Ruijter, W. P., & Van Leeuwen, P. J. (2002b). Upstream control of Agulhas ring shedding. *Journal of Geophysical Research*, *107*(C8), 23-1–23-11.

Schouten, M. W., De Ruijter, W. P. M., Van Leeuwen, P. J., & Dijkstra, H. A. (2002). An oceanic teleconnection between the equatorial and southern Indian Ocean. *Geophysical Research Letters*, *29*(16), 59-1–59-4. https://doi.org/10.1029/2001gl014542

Speich, S., Blanke, B., & Cai, W. (2007). Atlantic meridional overturning circulation and the Southern Hemisphere supergyre. *Geophysical Research Letters*, *34*(23). https://doi.org/10.1029/2007gl031583

Srinivasu, U., Ravichandran, M., Han, W., Sivareddy, S., Rahman, H., Li, Y., & Nayak, S. (2017). Causes for the reversal of North Indian Ocean decadal sea level trend in recent two decades. *Climate Dynamics*, *49*(11), 3887–3904. https://doi.org/10.1007/s00382-017-3551-y

Stammer, D., Anne, C., Ponte, R. M., & Tamisiea, M. E. (2013). Causes for contemporary regional sea level changes. *Annual Review of Marine Science*, *5*(1), 21–46. https://doi.org/10.1146/annurev-marine-121211-172406

Susanto, R. D., Gordon, A. L., & Zheng, Q. (2001). Upwelling along the coasts of Java and Sumatra and its relation to ENSO. *Geophysical Research Letters*, *28*(8), 1599–1602. https://doi.org/10.1029/2000GL011844

Thompson, P. R., Piecuch, C. G., Merrifield, M. A., McCreary, J. P., & Firing, E. (2016). Forcing of recent decadal variability in the Equatorial and North Indian Ocean. *Journal of Geophysical Research: Oceans*, *121*(9), 6762–6778. https://doi.org/10.1002/2016jc012132

Trenary, L. L., & Han, W. (2012). Intraseasonal-to-interannual variability of South Indian Ocean sea level and thermocline: Remote versus local forcing. *Journal of Physical Oceanography*, *42*(4), 602–627. https://doi.org/10.1175/jpo-d-11-084.1

Trenary, L. L., & Han, W. (2013). Local and remote forcing of decadal sea level and thermocline depth variability in the South Indian Ocean. *Journal of Geophysical Research: Oceans*, *118*(1), 381–398. https://doi.org/10.1029/2012jc008317

Tsujino, H., Urakawa, S., Nakano, H., Small, R. J., Kim, W. M., Yeager, S. G., et al. (2018). JRA-55 based surface dataset for driving ocean–sea-ice models (JRA55-do). *Ocean Modelling*, *130*, 79–139. https://doi.org/10.1016/j.ocemod.2018.07.002

Vinayachandran, P. N. M., Masumoto, Y., Roberts, M. J., Huggett, J. A., Halo, I., Chatterjee, A., et al. (2021). Reviews and syntheses: Physical and biogeochemical processes associated with upwelling in the Indian Ocean. *Biogeosciences*, *18*(22), 5967–6029. https://doi.org/10.5194/bg-18-5967-2021

Webster, P. J., Moore, A. M., Loschnigg, J. P., & Leben, R. R. (1999). Coupled ocean–atmosphere dynamics in the Indian Ocean during 1997–98. *Nature*, *401*(6751), 356–360. https://doi.org/10.1038/43848

Wirth, A., Willebrand, J., & Schott, F. (2002). Variability of the Great Whirl from observations and models. *Deep Sea Research Part II: Topical Studies in Oceanography*, *49*(7–8), 1279–1295. https://doi.org/10.1016/s0967-0645(01)00165-5

Yamagami, Y., Tozuka, T., & Qiu, B. (2019). Interannual variability of the natal pulse. *Journal of Geophysical Research: Oceans*, *124*(12), 9258–9276. https://doi.org/10.1029/2019jc015525

Yokoi, T., Tozuka, T., & Yamagata, T. (2008). Seasonal variation of the Seychelles Dome. *Journal of Climate*, *21*(15), 3740–3754. https://doi.org/10.1175/2008jcli1957.1

Zhou, L., Murtugudde, R., & Jochum, M. (2008). Dynamics of the intraseasonal oscillations in the Indian Ocean South Equatorial current. *Journal of Physical Oceanography*, *38*(1), 121–132. https://doi.org/10.1175/2007jpo3730.1

Zhuang, W., Feng, M., Du, Y., Schiller, A., & Wang, D. (2013). Low-frequency sea level variability in the southern Indian Ocean and its impacts on the oceanic meridional transports. *Journal of Geophysical Research: Oceans*, *118*(3), 1302–1315. https://doi.org/10.1002/jgrc.20129